Phase boundary engineering of metal-organic-framework-derived carbonaceous nickel selenides for sodium-ion batteries

Shiyao Lu[1,4,§], Hu Wu[1,§], Jingwei Hou[2,7], Limin Liu[1], Jiao Li[1], Chris J. Harris[2], Cheng-Yen Lao[2], Yuzheng Guo[5], Kai Xi[2,3] (✉), Shujiang Ding[1] (✉), Guoxin Gao[1] (✉), Anthony K. Cheetham[2,6], and R. Vasant Kumar[2]

[1] *Xi'an Key Laboratory of Sustainable Energy Materials Chemistry, MOE Key Laboratory for Nonequilibrium Synthesis and Modulation of Condensed Matter, State Key Laboratory of Electrical Insulation and Power Equipment, School of Chemistry, Xi'an Jiaotong University & Shaanxi Quantong Joint Research Institute of New Energy Vehicles Power, Xi'an Jiaotong University, Xi'an 710049, China*

[2] *Department of Materials Science and Metallurgy, University of Cambridge, Cambridge CB3 0FS, UK*

[3] *Cambridge Graphene Centre, Department of Engineering, University of Cambridge, Cambridge CB3 0FA, UK*

[4] *Department of Chemistry, City University of Hong Kong, Hong Kong 999077, Hong Kong, China*

[5] *School of Electrical Engineering and Automation, Wuhan University, Wuhan 430072, China*

[6] *Materials Research Laboratory, University of California, Santa Barbara, CA 93106, USA*

[7] *School of Chemical Engineering, University of Queensland, St Lucia, QLD 4072, Australia*

[§] *Shiyao Lu and Hu Wu contributed equally to this work.*

ABSTRACT

Sodium-ion batteries (SIBs) are promising power sources due to the low cost and abundance of battery-grade sodium resources, while practical SIBs suffer from intrinsically sluggish diffusion kinetics and severe volume changes of electrode materials. Metal-organic framework (MOFs) derived carbonaceous metal compound offer promising applications in electrode materials due to their tailorable composition, nanostructure, chemical and physical properties. Here, we fabricated hierarchical MOF-derived carbonaceous nickel selenides with bi-phase composition for enhanced sodium storage capability. As MOF formation time increases, the pyrolyzed and selenized products gradually transform from a single-phase Ni_3Se_4 into bi-phase $NiSe_x$ then single-phase $NiSe_2$, with concomitant morphological evolution from solid spheres into hierarchical urchin-like yolk-shell structures. As SIBs anodes, bi-phase $NiSe_x$@C/CNT-10h (10 h of hydrothermal synthesis time) exhibits a high specific capacity of 387.1 mAh/g at 0.1 A/g, long cycling stability of 306.3 mAh/g at a moderately high current density of 1 A/g after 2,000 cycles. Computational simulation further proves the lattice mismatch at the phase boundary facilitates more interstitial space for sodium storage. Our understanding of the phase boundary engineering of transformed MOFs and their morphological evolution is conducive to fabricate novel composites/hybrids for applications in batteries, catalysis, sensors, and environmental remediation.

KEYWORDS

metal organic frameworks, phase boundary, carbon nanotube, metal selenides, sodium ion batteries

1   Introduction

Rechargeable sodium-ion batteries (SIBs) are regarded as potential power sources for large-scale energy storage devices due to the low cost and abundance of sodium resources [1–4]. However, the large radius of the Na⁺ ion (0.98 Å compared with 0.69 Å for Li⁺) accounts for its intrinsically sluggish diffusion kinetics and severe volume changes, usually leading to unimpressive electrochemical performance [5, 6]. On account of these factors, numerous efforts have been devoted to developing stable electrodes in order to achieve good sodium storage ability. Among the various anode candidates, transitional metal sulfides [7–13], which store sodium via a conversion or alloy-dealloying reaction mechanisms, stand out for their impressive electronic conductivity and substantial theoretical capacity compared to hard carbon anodes (typically less than 300 mAh/g) [1, 14]. However, a "shuttle effect" generated by dissolution and diffusion of polysulfide ions occurs for most metal sulfides, leading to rapid capacity fading and poor cycle stability [15–17]. Compared to metal sulfides, metal selenides usually exhibit higher electronic conductivity and structural stability, and can thus present an improved cycle life and high rate performance with appropriate electrolytes operating within selected voltage window [18–20]. For example, Zhang and co-workers fabricated $FeSe_2$ cluster anodes which achieved 400 cycles at 1 A/g [21]. However, dramatic volume variations and severe aggregation still took place during long-term cycling, leading to undesirable cycle performance for the metal selenides.

In order to stabilize the structures, avoid agglomeration and further enhance the conductivity of metal selenides-based anodes, one efficient strategy that has been frequently adopted is to fabricate carbonaceous composites with porous morphologies by hybridizing electroactive metal chalcogenides with carbon matrixes, such as hollow carbon spheres, graphene and carbon nanotubes (CNTs) [22–27]. Wu et al. proposed

an epitaxial growth strategy to obtain hierarchical porous CoSe-rGO hybrids with enhanced mechanical strength while suppressing the dissolution of Se [28]. Confining electroactive materials within a conductive carbon matrix can significantly enhance structural stability and shorten Na$^+$ ion diffusion lengths during repeated charge–discharging cycling. Moreover, this strategy maintains their original morphology after continuous cycling, resulting in enhanced capacity and cycling stability [29, 30]. In a related development, it has been found that metal-organic frameworks (MOFs) can be efficiently converted [31–34], by means of a facile calcination or pyrolysis treatment, into nanostructured carbonaceous metal chalcogenide composites, which have exhibited excellent electrochemical properties in lithium-ion batteries (LIBs), SIBs and Li-S batteries [35–42]. This is because the carbonized and graphitized carbon generated by *in situ* calcination encapsulates the electroactive material, significantly alleviating the volume expansion during repeated sodiation/desodiation whilst simultaneously proving good electronic conductivity [43]. Recent work has shown that the carbonization of MOFs can be sensitive to both their morphology and the pyrolysis reaction conditions. For example, the morphology of MOFs can be tuned by using different synthesis conditions such as temperature, time, ligands and the ratios of reactants [44, 45]. Adjusting such reaction parameters has been used to maximize the porosity of MOFs, leading to enhanced energy storage capability. In addition, other recent research indicates that carbonizing MOFs by a low temperature pyrolysis process using reducing gas enables a two-step reaction: First, metal nanocatalysts are generated from internal metal ions, and second, CNTs are produced from residual organic units [46]. By employing this method, a series of MOF-derived CNT-assembled composites with different morphologies could be fabricated with hierarchical pores and high specific surface area. A further selenization step on the product can turn the carbonized MOF into CNT-confined metal selenides that have high capacities that can be exploited in energy storage. For example, Qiu's group successfully prepared CNT-bridged carbon CoSe$_2$ nanospheres, which delivered a high reversible capacity of 470 mAh/g at 0.2 A/g [41]. This work elucidated the importance of developing metal selenide composites with interior void space and a

conductive network for high-performance sodium electrode materials. In addition, biphasic selenides exhibit higher electronic conductivities and richer redox reactions when compared to monophasic selenides, which can further improve the electrochemical performance [47].

Herein, we systematically study the morphological evolution of Ni-BTC MOF (BTC = benzenetricarboxylic acid) and their transformed nanostructures for energy storage applications [46]. As the hydrothermal synthesis time was gradually increased from 3 to 15 h, the Ni-BTC MOFs (denoted as Ni-MOF-3h, Ni-MOF-5h, Ni-MOF-10h and Ni-MOF-15h, respectively) grow from solid spheres into hollow urchin-like shapes. Subsequent low temperature pyrolysis then transforms the Ni-MOF samples into carbon-confined metallic Ni nanoparticles, which further catalyzes the *in-situ* formation of extruded CNTs from the 5, 10, 15h Ni-BTC samples (denoted as Ni@C-3h, Ni@C/CNTs-5h, Ni@C/CNTs-10h, Ni@C/CNTs-15h, respectively). After a simple selenization process, solid Ni@C-3h samples are transformed into a Ni$_3$Se$_4$ phase, while Ni@C/CNTs-15h converts into a NiSe$_2$ phase. As the carbonization time of the Ni-BTC samples increases, the final selenized products gradually transform from Ni$_3$Se$_4$ into NiSe$_2$ (denoted as Ni$_3$Se$_4$@C-3h, NiSe$_x$@C/CNTs-5h, NiSe$_x$@C/CNTs-10h, NiSe$_2$@C/CNTs-15h, respectively). The nanocomposites with highly active phase boundary exhibit excellent performance as anodes in sodium batteries: for example, NiSe$_x$@C/CNT-10h provides a high reversible capacity (387.1 mAh/g at 100 mA/g) and ultralong cycling performance 306.3 mAh/g at 1 A/g after 2,000 cycles). Further exploration of this morphological evolution will allow the development of new classes of hybrid materials with hierarchical nanostructures for applications in batteries, sensors and catalysts.

2 Results and discussion

Figure 1 presents the schematic diagram of the morphology evolution of the Ni-BTC MOFs with reaction time and the corresponding synthesis of nickel selenide/carbon composites. Initially, Ni-BTC MOFs were fabricated through a hydrothermal reaction with a mixture of nickel nitrate, trimesic acid and polyvinylpyrrolidone (PVP) (acting as a metal source, organic ligand and stabilizing agent, respectively) [44]. The reaction
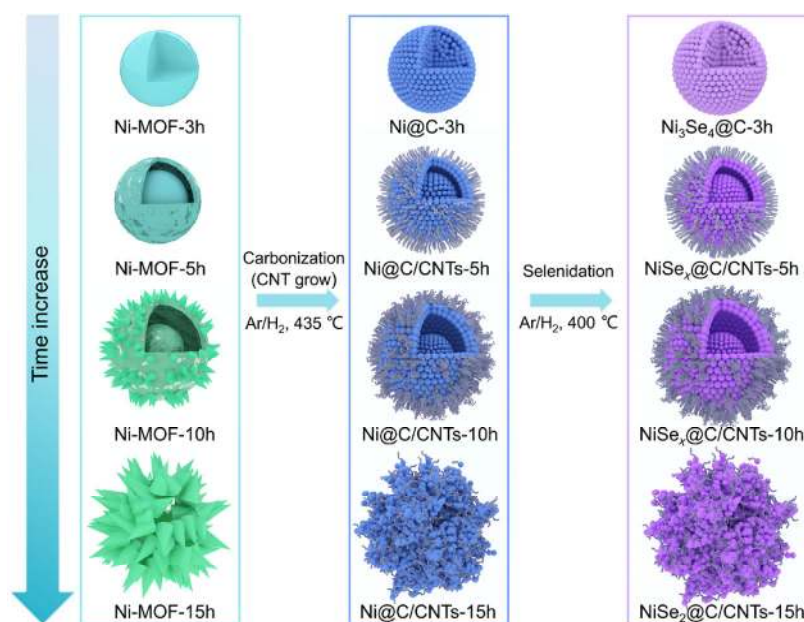

Figure 1 Schematic illustrations for the evolution of Ni-MOF in different hours and strategy for fabricating nickel selenides/carbon composites used as anode materials for SIBs.

time was precisely regulated from 3 to 15 h to understand the evolution of this process. The morphological evolution of Ni-BTC MOFs with time was first characterized by field emission scanning electron microscopy (FESEM) and transmission electron microscopy (TEM). As shown in Figs. 2(a)–2(h), both Ni-MOF-3h and Ni-MOF-5h samples have a spherical structure with diameters in the range of 1.2 to 1.6 μm. Ni-MOF-5h samples, however, exhibit an inconspicuous hollow structure and a rough surface in comparison to the solid Ni-MOF-3h samples. As the reaction time extends to 10 h, a typical Ostwald ripening process, which leads to a hierarchical core-shell structure with staggered nanorods emerging from its external shell, is observed [48]. The nanorods continue to grow as the reaction time increases. After 15 h, the Ni-MOF-15h samples transform into an urchin-like structure, whilst some nanorods collapse, indicating the instability of the samples. X-ray diffraction (XRD) analysis of the above samples demonstrated that the Ni-BTC MOFs gradually transform from amorphous to crystalline materials during the solvothermal reactions (Fig. S1 in the Electronic Supplementary Material (ESM)).

Subsequently, the Ni-BTC MOFs were annealed under Ar/H$_2$ flow at 435 °C for 8 h to obtain CNTs-connected carbon-coated nickel nanospheres. The pyrolyzed MOFs reveal two distinct morphologies (Figs. 2(i)–2(l) and Fig. S2 in the ESM). For the solid Ni@C-3h sample, the Ni-MOF-3h is reduced into numerous graphitic carbon-enclosed nickel nanoparticles with diameters in the range of 5–30 nm. For the rest of the samples, we succeed in inducing the residual organics from the external shell and nanorods to form oriented CNT structures containing nickel nanoparticles. These CNTs possess outer diameters ranging from 15 to 20 nm, in which crystalline nickel nanoparticles are encapsulated. It is also observed that some of the shell structure in the Ni@C/CNTs-15h sample almost detached from the main body, generating clusters of CNTs attached to the inner core. The XRD analysis and the energy dispersive X-ray (EDX) spectroscopy results of the above four samples demonstrate the existence of metallic nickel and graphite (Figs. S3 and S4 in the ESM). In particular, the surface carbon ratios in the four samples reveal increasing concentrations, which is attributed to the increasing CNT content.

Lastly, the Ni@C and Ni@C/CNT composites were selenized by a post-pyrolysis process under an H$_2$Se airflow generated from the reaction of H$_2$ and Se powders, resulting in Ni$_3$Se$_4$@C

and NiSe$_x$@C/CNTs composites [41]. The corresponding TEM and FESEM images are illustrated in Figs. 3(a)–3(h), which show that the samples almost maintain their former morphologies. Furthermore, elemental mapping images (Figs. 3(i)–3(l)) performed on the high-angle annular dark field, scanning transmission electron microscopy (HADDF-STEM) confirmed the uniform elemental distributions in all four samples, implying a complete selenization process. In addition, EDX spectroscopy results (Fig. S5 in the ESM) of the selenized samples detected Ni, Se and C elements in the hybrid structures. Notably, the atomic ratio of C to Se increases gradually, indicating inconsistent element contents across the four samples.

To verify the specific crystallinity of the four composites, XRD analysis was performed (Fig. 4(a)). Interestingly, selenization is not uniform across the four samples; that is to say, both wilkmanite Ni$_3$Se$_4$ (JCPDS card no.18-0890) and penroseite NiSe$_2$ (JCPDS card no.88-1711) are detected as the main components [49]. The selenization process of the solid Ni@C-3h sample only occurs partially, leading to the formation of a lower Se content Ni$_3$Se$_4$@C-3h composite, in contrast to the other samples which are dominated by NiSe$_2$. As the hydrothermal reaction time increases, the predominant peak at 45.1° (corresponding to the ($\bar{1}$14) reflection) from Ni$_3$Se$_4$ decreases gradually, which is associated with the appearance of characteristic NiSe$_2$ peaks at 29.8° and 36.6° (corresponding to the (220) and (221) reflections). More specifically, the XRD patterns and crystal structures of NiSe$_2$ and Ni$_3$Se$_4$ are displayed in Fig. S6 in the ESM, separately. We conclude from the XRD results that the 5 and 10 h samples contain both Ni$_3$Se$_4$ and NiSe$_2$, and that the 15 h samples contain almost pure NiSe$_2$ with trace Ni$_3$Se$_4$. They are denoted as NiSe$_x$@C/CNTs-5h, NiSe$_x$@C/CNTs-10h and NiSe$_2$@C/CNTs-15, respectively. Furthermore, the crystal structures of Ni$_3$Se$_4$@C-3h and NiSe$_x$@C/CNTs-10h were also studied by high-resolution TEM (HRTEM) and selected area electron diffraction (SAED) analysis. As shown in Figs. 4(d)–4(h), the sizes of the Ni$_3$Se$_4$ nanoparticles are in the range of 20–50 nm with several graphitic carbon layers, while the CNT-bridged NiSe$_x$ nanoparticles reveal a smaller size of 10–45 nm. An interplanar distance of 0.202 and 0.269 nm are detected in Ni$_3$Se$_4$@C-3h and NiSe$_x$@C/CNTs-10h samples, corresponding to the dominant ($\bar{1}$14) and (210) planes of Ni$_3$Se$_4$ and NiSe$_2$, respectively. Furthermore, a phase boundary can be observed between (211) facet of NiSe$_2$ and ($\bar{1}$14) facet of
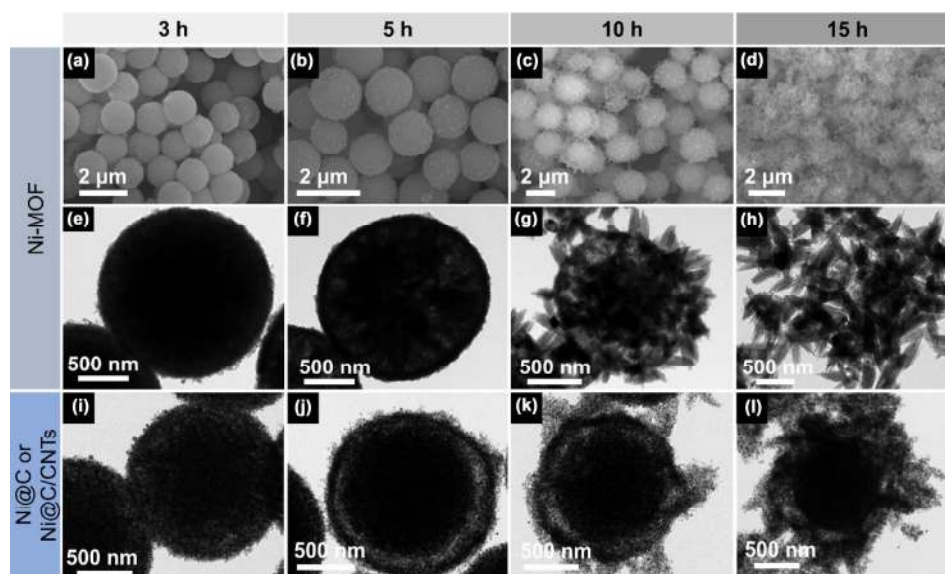

Figure 2 FESEM and TEM images of ((a) and (e)) Ni-MOF-3h; ((b) and (f)) Ni-MOF-5h; ((c) and (g)) Ni-MOF-10h; ((d) and (h)) Ni-MOF-15h. TEM images of (i) Ni@C-3h; (j) Ni@C/CNTs-5h; (k) Ni@C/CNTs-10h; (l) Ni@C/CNTs-15h.
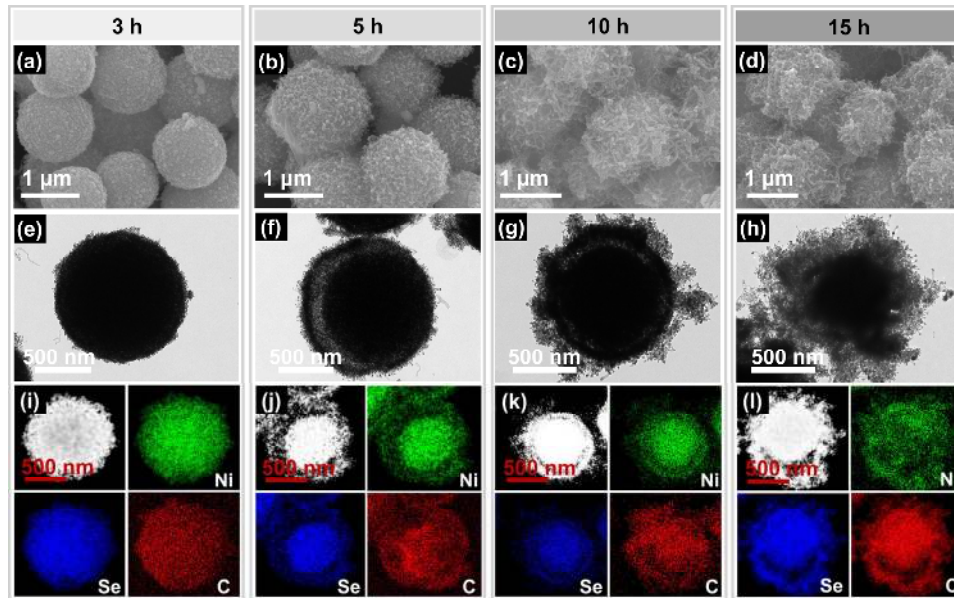
Figure 3 FESEM, TEM, HAADF-STEM and corresponding elemental mapping images of ((a), (e) and (i)) Ni$_3$Se$_4$@C-3h; ((b), (f) and (j)) NiSe$_x$@C/CNTs-5h; ((c), (g) and (k)) NiSe$_x$@C/CNTs-10h; ((d), (h) and (l)) NiSe$_2$@C/CNTs-15h.
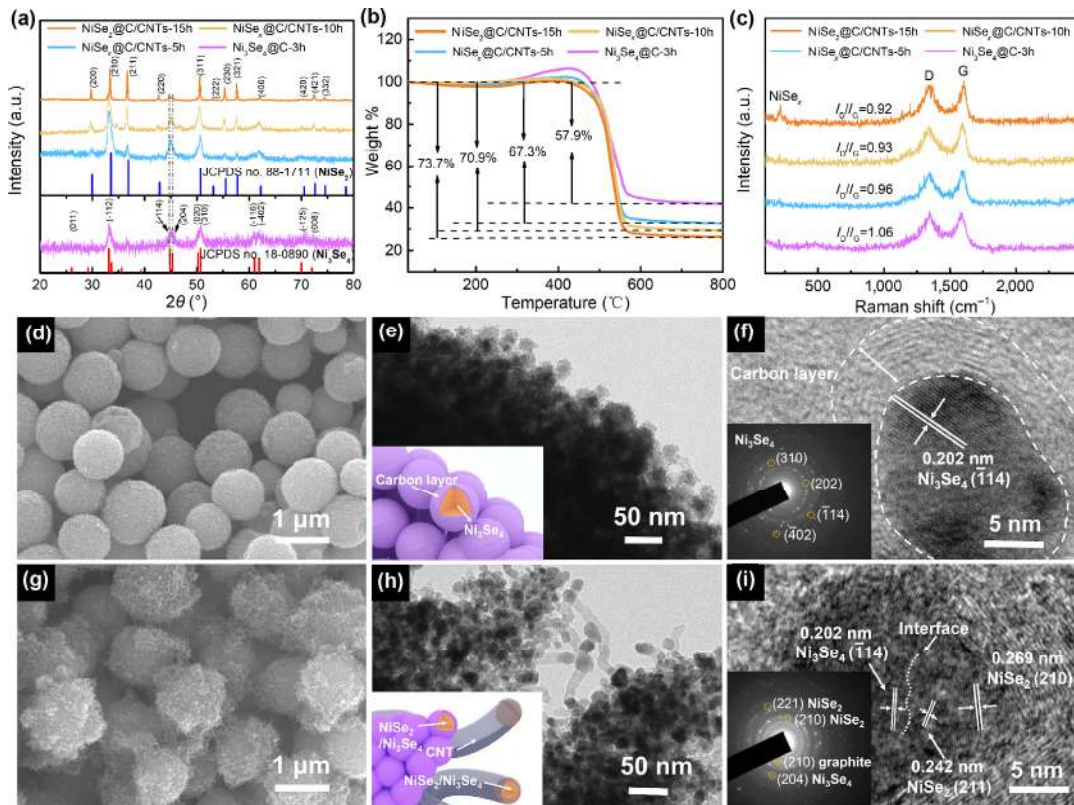

Figure 4 Characterization of various nickel selenides/carbon composites. ((a)–(c)) XRD patterns, TGA curves and Raman spectra of Ni$_3$Se$_4$@C-3h, NiSe$_x$@C/CNTs-5h, NiSe$_x$@C/CNTs-10h, NiSe$_2$@C/CNTs-15h; SEM, TEM, HRTEM and SAED images of ((d)–(f)) Ni$_3$Se$_4$@C-3h, ((g)–(i)) NiSe$_x$@C/CNTs-10h.

Ni$_3$Se$_4$, demonstrating a lattice mismatch between two phases. The SAED patterns of two samples also reveal a polycrystalline feature and the intense diffraction rings are readily indexed as monoclinic Ni$_3$Se$_4$ and cubic NiSe$_2$, which is in a good agreement with the XRD results.

The total carbon content in the four composites was determined by thermogravimetric analysis (TGA). As displayed in Fig. 4(b), the TGA curves first display a weight loss due to the loss of water from 25 to 200 °C. The weight gain that follows, between 200 to 432 °C, can be credited to the oxidation of Ni$_3$Se$_4$ and NiSe$_2$, generating NiO and SeO$_2$. An abrupt weight

loss emerges once the temperature is over ~ 430 °C, which is due to the volatilization of SeO$_2$ and the generation of CO$_2$. The total reaction is summarized as: Ni$_x$Se@C + O$_2$ → xNiO + SeO$_2$↑ + CO$_2$↑ [43]. We assume that Ni$_3$Se$_4$@C-3h and NiSe$_2$@C/CNTs-15h are pristine Ni$_3$Se$_4$@C and NiSe$_2$@C composites, respectively, and that the other samples are Ni$_3$Se$_4$@NiSe$_2$@C hybrid composites. Therefore, the carbon content in the four samples can be approximately estimated as being between 7.6% and 23.8%, revealing an increasing carbon content from Ni$_3$Se$_4$@C-3h to NiSe$_2$@C/CNTs-15h. Figure 4(c) gives the Raman spectra of the four composites. The minor peak

at 208.3 cm^{-1} is ascribed to the A$_g$ mode of Ni$_x$Se [49]. Two additional peaks emerge at 1,348.7 (D band) and 1,601.5 cm^{-1} (G band), which are associated with disordered carbon and graphitic carbon, respectively. Remarkably, The I_D/I_G ratio decreases from 1.06 to 0.92 across the four samples, demonstrating the existence of graphitic carbon grown from CNTs.

In order to further understand the differences in chemical composition and valence states between Ni$_3$Se$_4$ and NiSe$_2$, X-ray photoelectron spectroscopy (XPS) was conducted on the Ni$_3$Se$_4$@C-3h and NiSe$_2$@C/CNTs-15h samples and their Se 3d spectra are shown in Fig. S7 in the ESM. In general, four main peaks at 54.3, 55.0, 55.6 and 59.2 eV can be deconvoluted in both samples, corresponding to Se 3d$_{5/2}$, Se 3d$_{3/2}$, Se-Se and Se-O, respectively. However, the Ni$_3$Se$_4$@C-3h samples reveal enhanced Se 3d$_{5/2}$ and decreased Se-Se peak intensity compared with NiSe$_2$@C/CNTs-15h samples, which could be ascribed to the greater weighting from the Se-Se bond in NiSe$_2$. The porosities and pore size distributions of the as-prepared hybrid composites were estimated by Brunauer–Emmert–Teller (BET) analysis. As shown in Fig. S8 in the ESM, the distinct hysteresis loops between the adsorption and desorption curves imply the presence of porous structure within all samples. The solid Ni$_3$Se$_4$@C-3h sample presents the lowest surface area of 64.1 m^2/g with an average pore size at 32.3 nm. As the samples change from a solid structure to a hollow CNT-bridged structure, an enlarged surface area and decreased pore size are obtained. Thus, the NiSe$_2$@C/CNTs-15h sample exhibits the largest surface area of 108.1 m^2/g with an average pore size at 8.6 nm.

The electrochemical performances of the four nickel selenide composites for SIBs were evaluated by assembling them into coin-type half-cells. In accordance with previous reports, the voltage window was modified to 0.5–2.9 V in order to avoid side reactions [50]. Figure S9 in the ESM displays the cycling performance of the four samples at a current density of 1 A/g. All four samples reveal excellent cycling stability with differing specific capacities. We therefore performed rate performance measurements on the nickel selenide nanocomposites, as displayed in Fig. 5(a). As with the results of the cycling performance, NiSe$_x$@C/CNTs-10 possesses the best rate performance among the four samples. The specific capacities of NiSe$_2$@C/CNTs-15 and NiSe$_x$@C/CNTs-5h are slightly lower than that of NiSe$_x$@C/CNTs-10h, while Ni$_3$Se$_4$@C-3h has the lowest specific capacity. As the current density increases from 0.1 to 0.2, 0.5, 1.0, 2.0, 5.0 and 10.0 A/g, the reversible discharge capacity of NiSe$_x$@C/CNTs-10h gradually changes from 387.1 to 357.8, 334.5, 321.2, 306.6, 282.7 and 258.4 mAh/g, respectively. When it is reset to 1 A/g after 70 cycles, the discharge capacity rapidly recovers to 322.5 mAh/g, indicating the superb high-rate performance of NiSe$_x$@C/CNTs-10. However, the discharge capacity of Ni$_3$Se$_4$@C-3 was only 283.7 and 99.8 mAh/g at 0.1 and 10 A/g, respectively. Such behavior can be ascribed to the different phase contents of Ni$_3$Se$_4$, NiSe$_2$ and carbon in the four samples. As the reaction time increased from 3 to 15 h, the Ni-BTC MOF gradually transformed from a solid structure into a hollow yolk-shell structure. This latter structure is more likely to undergo a complete selenization process, leading to higher NiSe$_2$ contents in the composite products; we also note that NiSe$_2$ has a larger theoretical capacity than Ni$_3$Se$_4$. We shall conclude that NiSe$_x$@C/CNTs-10h exhibits the best rate performance and the highest discharge specific capacity among the four samples on account of its optimal balance between internal cavity structure and biphasic composition.

Subsequently, we studied the electrochemical performance of the NiSe$_x$@C/CNTs-10h sample in greater detail. The
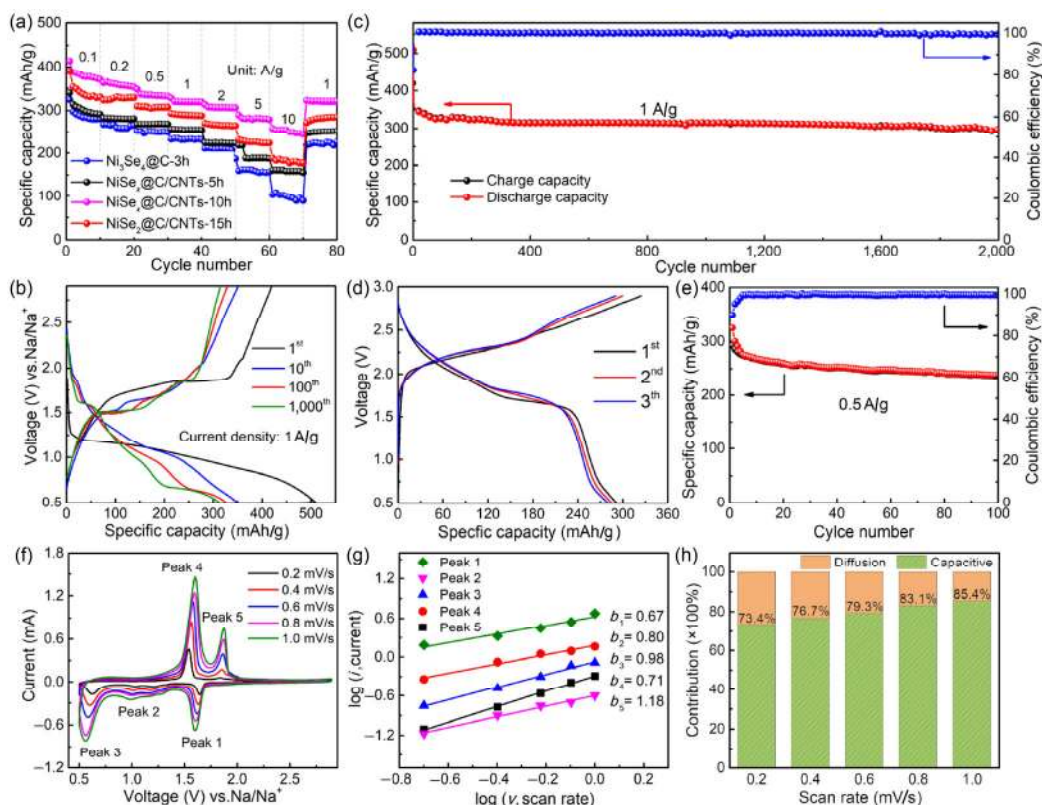

Figure 5 Electrochemical performance of the four nickel selenides nanocomposites in the cut-off voltage range 0.5–2.9 V. (a) Charge–discharge curves of NiSe$_x$@C/CNTs-10h at different cycle numbers at 1 A/g. (b) Cycling stability of NiSe$_x$@C/CNTs-10 at 1 A/g. (c) Rate capability evaluated at various current densities ranging from 0.1 to 10 A/g. (d) Charge and discharge profiles. (e) Cycling performance and Coulombic efficiency of the NiSe$_x$@C/CNTs-10//NVP full cells at 0.5 A/g. (f) CV profiles of NiSe$_x$@C/CNTs-10h at different scan rates. (g) Corresponding log i versus log v plot at each redox peak. (h) Pseudocapacitive contribution at a scan rate of 1 mV/s.

corresponding discharge and charge profiles at a current density of 1 A/g are displayed in Fig. 5(b). The initial discharge and charge capacities are 509.3 and 419.4 mAh/g, respectively, yielding an initial coulombic efficiency of 82.3%. The irreversible capacity loss in the first cycle is mainly ascribed to the irreversible decomposition of electrolyte and the formation of a solid-electrolyte interface (SEI) layer [51, 52]. Notably, the initial charge and discharge profiles are rather different from those that followed, which is mostly attributed to the activation of nickel selenide and side reactions that make initial sodiation and desodiation unstable [50, 53]. The discharge and charge curves however almost overlap after 100 cycles and stable discharge plateaus at 1.60, 1.03, 0.65 V and charge plateaus at 1.53, 1.86 V are well maintained. Figure 5(c) shows the long-term cycle performance of NiSe$_x$@C/CNTs-10h at 1 A/g. Even after 2,000 cycles, the discharge capacity remains at 306.3 mAh/g with a capacitance decay ratio of only 0.01% per cycle. In addition, the Coulombic efficiency of NiSe$_x$@C/CNTs-10h remains above 99.6% after the fourth discharge/charge cycle, indicating excellent energy conversion efficiency. For comparison, we also investigate the electrochemical performance of Ni$_3$Se$_4$@C-3h, as shown in Fig. S10 in the ESM. Unlike NiSe$_x$@C/CNTs-10h, almost no evident plateaus are observed, indicating an incomplete electrochemical reaction process. A lower discharge capacity of 242.8 mAh/g is achieved after 2,000 cycles. The outstanding electrochemical performance of our NiSe$_x$@C/CNTs-10h is compared with other nickel selenide anodes in Table S1 in the ESM, demonstrating its advantageous long cyclic stability and high rate performance. Additionally, the practical value of NiSe$_x$@C/CNTs-10h was evaluated in full cells with Na$_3$V$_2$(PO$_4$)$_3$ (NVP) as the cathode. The flower-like NVP delivers a stable reversible capacity of 95.4 mAh/g at 1 C in a half-cell (Fig. S11 in the ESM). The NVP//NiSe$_x$@C/CNTs-10 full cells showed a remarkable discharge capacity of 238.5 mAh/g at 0.5 A/g after 100 cycles with a discharge plateau of 2.0 V (Figs. 5(d) and 5(e)), demonstrating the potential of NiSe$_x$@C/CNTs-10h as an anode for high-performance sodium ion batteries.

It has been reported that the high-rate performance of electrode materials is related to its potential pseudocapacitive behavior upon continuous discharge/charge cycling. In order to explore the electrochemical reaction dynamics of NiSe$_x$@C/CNTs-10h, we measured its cyclic voltammetry (CV) curves at various scan rates from 0.2 to 1.0 mV/s between 0.5 and 2.9 V (Fig. 5(f)). Generally, the peak current (i) and scan rate (v) obey the following equations [19]
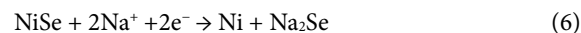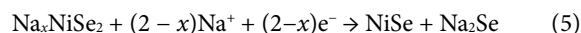
$$i = av^b \tag{1}$$

$$\log(i) = \log(a) + b \cdot \log(v) \tag{2}$$

where a and b are adjustable parameters, and b is determined from the slope of the log(i) vs. log(v) plot. Normally, when $b = 0.5$, the electrochemical sodium storage reaction is controlled by ionic diffusion. However, as b approaches 1.0, the sodium storage process is dominated by pseudocapacitance. As shown in Fig. 5(g), the b-values (fitted slopes) of the plots from the five peaks in Fig. 5(f) are 0.67, 0.80, 0.98, 0.71 and 1.18. These results show that pseudocapacitive behavior dominates the repeated redox processes, giving rise to rapid Na$^+$ intercalation/extraction kinetics. Furthermore, the total pseudocapacitive contribution can be calculated according to the equation: $i = k_1v + k_2v^{0.5}$ [54], where k_1v and $k_2v^{0.5}$ represent the pseudocapacitive and ionic diffusion contributions, respectively. As presented in Fig. 5(h), the total pseudocapacitive contribution of the NiSe$_x$@C/CNTs-10 increased from 73.4% to 85.4% as the scan rates increased from 0.2 to 1.0 mV/s. This result is similar to that of other metal sulfides/selenides [18, 55]. Our results demonstrate
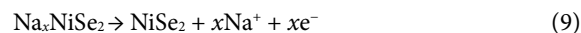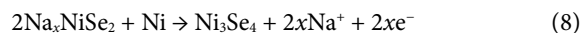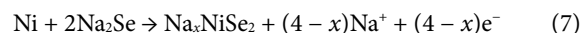
that pseudocapacitive behavior provides a major capacitance contribution, especially at high scan rates, on account of the unique CNT-bridged yolk-shell structure effectively reducing the diffusion path. For comparison, the pseudocapacitive behavior of Ni$_3$Se$_4$@C-3h was also evaluated, as shown in Fig. S12 in the ESM. Again, five distinct current peaks are detected at the same voltages, though the peak intensities are relatively smaller. The b-values of the five peaks are close to those of the NiSe$_x$@C/CNTs-10h sample, indicating partial pseudocapacitive behavior during the electrochemical process. However, as shown in Figs. S12(c) and S12(d) in the ESM, the pseudocapacitive contributions of Ni$_3$Se$_4$@C-3h are lower than those of NiSe$_x$@C/CNTs-10h, mainly due to the sluggish electrochemical reaction between Na$^+$ ions and Ni$_3$Se$_4$@C-3h. Furthermore, the effects of the voltage window and the electrolyte have been also systematically studied (Figs. S13–S15 in the ESM)

To further understand the possible sodiation/desodiation mechanisms of NiSe$_x$@C/CNTs-10h, *ex-situ* XRD, SAED, HRTEM, electrochemical impedance spectroscopy (EIS) and SEM measurements were performed at different stages of the electrochemical reaction (Figs. 6(a)–6(e), Figs. S16 and S17 in the ESM). Figure 6(a) presents the *ex-situ* XRD patterns of the NiSe$_x$@C/CNTs-10h electrodes at several charge/discharge stage. As the discharge voltage decreases from the initial potential value of 1.9 to 0.5 V, the typical diffraction peaks of cubic NiSe$_2$ and monoclinic Ni$_3$Se$_4$ diminish gradually before vanishing completely. At the same time, the weak diffraction peaks that emerge at 37.2°, 44.0° and 44.5° can be assigned to the (220) and (311) planes of Na$_2$Se (JCPDS No.47-1699) and the (111) plane of metallic Ni (JCPDS No.04-0850), respectively [49]. During the subsequent charging process from 0.5 to 2.9 V, the strong characteristic diffraction peaks of NiSe$_2$ and Ni$_3$Se$_4$ gradually recover, while those of Ni and Na$_2$Se gradually disappear. The presence of these intermediates was further verified by *ex-situ* SAED patterns and HRTEM images. The *ex-situ* SADE (Fig. 6(b)) clearly discloses the polycrystalline diffraction rings of the (220) and (400) planes of Na$_2$Se, the (111) plane of Ni, and (003) plane of graphite when discharged to 0.5 V. The lattice fringes of these discharge intermediates are also shown in Fig. 6(c). After the cell was recharged to 2.6 V once more, the *ex-situ* SAED (Fig. 6(d)) and *ex-situ* HRTEM (Fig. 6(e)) reveal the typical diffraction rings and lattice planes of NiSe$_2$ and Ni$_3$Se$_4$, respectively, indicating a completely reversible reaction process. Based on the above results and the reported literature [50, 56], the possible reaction mechanism for the electrochemical behavior of NiSe$_x$@C/CNTs-10h can be summarized as follows

Discharge process:

$$\text{NiSe}_2 + x\text{Na}^+ + x\text{e}^- \rightarrow \text{Na}_x\text{NiSe}_2 \tag{3}$$

$$\text{Ni}_3\text{Se}_4 + 2x\text{Na}^+ + 2x\text{e}^- \rightarrow 2\text{Na}_x\text{NiSe}_2 + \text{Ni} \tag{4}$$

$$\text{Na}_x\text{NiSe}_2 + (2-x)\text{Na}^+ + (2-x)\text{e}^- \rightarrow \text{NiSe} + \text{Na}_2\text{Se} \tag{5}$$

$$\text{NiSe} + 2\text{Na}^+ + 2\text{e}^- \rightarrow \text{Ni} + \text{Na}_2\text{Se} \tag{6}$$

Charge process:

$$\text{Ni} + 2\text{Na}_2\text{Se} \rightarrow \text{Na}_x\text{NiSe}_2 + (4-x)\text{Na}^+ + (4-x)\text{e}^- \tag{7}$$

$$2\text{Na}_x\text{NiSe}_2 + \text{Ni} \rightarrow \text{Ni}_3\text{Se}_4 + 2x\text{Na}^+ + 2x\text{e}^- \tag{8}$$

$$\text{Na}_x\text{NiSe}_2 \rightarrow \text{NiSe}_2 + x\text{Na}^+ + x\text{e}^- \tag{9}$$

Calculations based on density functional theory (calculation method was shown in the ESM) were performed to further study the Na insertion at the interface between Ni$_3$Se$_4$ and NiSe$_2$. In Fig. 6(f), the insertion energies of Na interstitials into pure Ni$_3$Se$_4$, pure NiSe$_2$, and at their interface have been compared. The large positive insertion energy leads to a low concentration of Na diffused into bulk NiSe$_2$ and Ni$_3$Se$_4$.
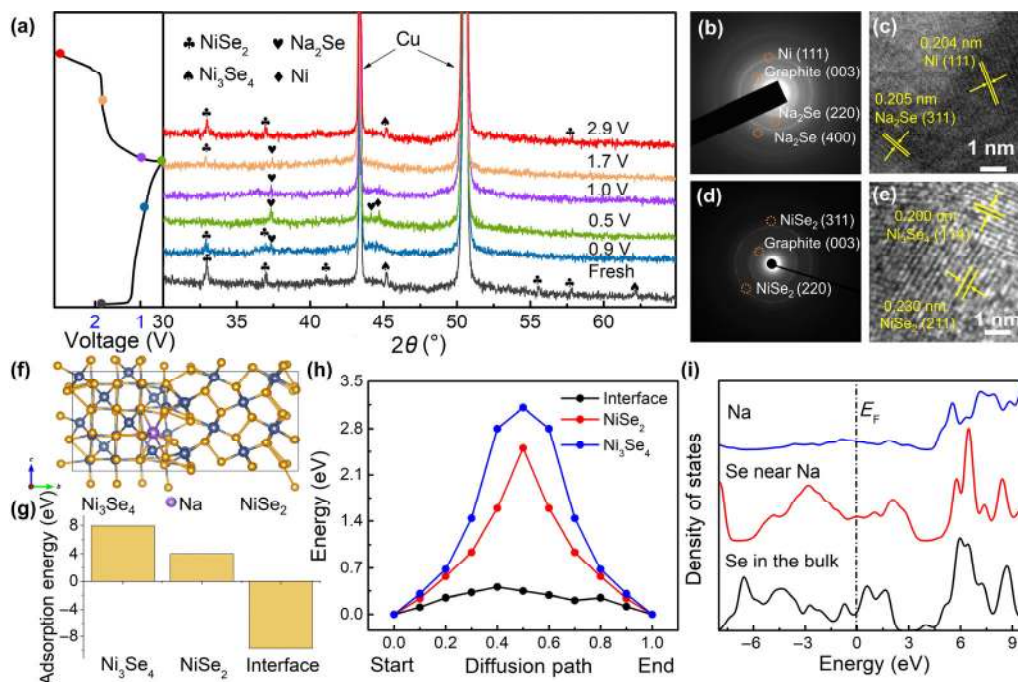
Figure 6 Reaction mechanism: (a) *ex-situ* XRD analysis of the NiSe$_x$@C/CNTs-10h electrodes at different charge/discharge states and *ex-situ* SAED, HRTEM of NiSe$_x$@C/CNTs-10h at different cycling stages: ((b), (c)) discharge to 0.5 V, ((d), (e)) charge to 2.6 V, (f) scheme of Na$^+$ transfer in phase boundary, (g) calculation of the Na$^+$ adsorption energy of Ni$_3$Se$_4$, NiSe$_2$ and the interface, (h) the energy minimum diffusion pathway of a Na atom along the interface, (i) calculated density of states (DOS) of Na, Se near Na, and Se at the interface as shown in (f).

However, the large negative insertion energy of Na at the interface suggests that Na tends to spontaneously diffuse into the interfacial area between the two selenides. We also estimated the diffusion barrier of Na at the interface to be around 0.41 eV, whereas the diffusion barrier in pure NiSe$_2$ and Ni$_3$Se$_4$ is larger than 3.0 eV, as shown in Fig. 6(g). This confirms that diffusion along interfaces or grain boundaries is preferable. In Fig. 6(h), the atomic structure of Na at the interface is shown, as well as the diffusion path of Na along the interface. The lattice mismatch at the interface creates a large strain field which helps to accommodate the extra Na atom. The insertion of Na significantly affects the local atomic structure. Hirshfield analysis confirms that there is charge transfer of 0.12 eV between Na and neighboring Se atoms. Therefore, Na has a strong interaction with the interface region in Ni$_3$Se$_4$ and NiSe$_2$. The DOS around the Fermi level of Se at the interface near Na atoms has been completely changed compared with the bulk ones, indicating a strong interaction of the Na with the interfacial atoms. This atomic and electronic interaction could lead to higher insertion concentrations and large charge transfer, both of which facilitate sodium storage at the interface region.

3   Conclusions

Four types of Ni-BTC MOFs with contrasting morphologies were fabricated via a facile solvothermal reaction using different reaction times. The results show that the morphologies of the Ni-BTC precursors gradually changed from solid spheres to hollow urchins as the solvothermal time increased from 3 to 15 h. After subsequent pyrolysis followed by selenization, four carbon-coated or CNT-bridged metal selenide composites were obtained. These showed a gradual evolution from Ni$_3$Se$_4$ to NiSe$_2$ as a function of the original MOF synthesis time. When used as anodes in SIBs, NiSe$_x$@C/CNTs-10h exhibited a high specific capacity, long cycle stability, and high rate performance. The interface between Ni$_3$Se$_4$ and NiSe$_2$ lowers the Na$^+$ insertion energy, facilitating the reaction kinetics during electrochemical

cycling. CNT-bridged yolk-shell composites have unique nano-structures that combine the porous features from the MOF-derived materials with the advantages of CNTs. The hollow porous structure provides protection against volume changes, whilst the CNTs introduce a large number of mesopores, shortening charge transfer paths and improving the utilization efficiency of the active materials. The above results demonstrate that the use of MOF-derived carbons combined with selenization provides an effective route for synthesizing metal selenide nanocomposites and offers a novel strategy for obtaining high-performance electrode materials.

4   Experimental methods

4.1   Synthesis of graphitic carbon-coated Ni$_3$Se$_4$ nanosphere hybrids (Ni$_3$Se$_4$@C) and CNT-bridged carbon-coated NiSe$_2$ nanospheres (NiSe$_2$@C/CNTs)

All chemical reagents are analytically pure and purchased from Aladdin Chemical Co. Ltd, China. The Ni-BTC was synthesized by a typical hydrothermal method. First, ethanol, N, N-dimethylformamide (DMF) and deionized water with a volume ratio of 1:1:1 were mixed to form 30 mL mixed solution. Then, 432 mg of Ni(NO$_3$)$_2$·6H$_2$O, 150 mg of 1,3,5-benzenetri-carboxylic acid (H$_3$BTC) and 1.5 g of polyvinylpyrrolidone (PVP, K-36) were dissolved in the prepared mixture with continuous stirring for 30 min. The obtained solution was transferred into a 50 mL Teflon-lined autoclave and heated to 150 °C respectively for 3, 5, 10, 15 h to obtain four products with different morphology. The green products were collected by centrifugation and washed by deionized water and ethanol several times, then dried in an oven at 60 °C overnight. Next, the four precursors were annealed under a mixed H$_2$/Ar flow with 5 vol% H$_2$ at 435 °C for 8 h with a heating rate of 2 °C/min to obtain four Nickel-carbon composites. Finally, the selenization process was accomplished by placing the

nickel-carbon composites and excessive selenium powder separately on both sides of the porcelain and annealed under the H_2/Ar flow at 400 °C for 3 h.

4.2 Material characterization

The morphology of as-prepared composites was characterized by FESEM (JEOL JSM-6700F) and TEM (JEOL; JEM-2100F). EDX measurements were performed on an FEI Quanta 250 FEG SEM. X-ray diffraction (XRD; Bruker AXS D8 Advance) to acquire the crystallographic information. The total carbon content was obtained by thermogravimetric analysis (Perkin-Elmer TGA 7) carried out under an air flow of 200 mL/min with a heating rate of 10 °C/min. The chemical compositions of samples were investigated by XPS measurements, performed on ESCALab 250 (USA) with monochromatic Al K sources. To obtain the specific surface area and pore size distribution of composites, N_2 sorption measurements and the BET method (ASAP 2020 PLUS HD88) were employed. Raman spectra were collected by a laser Raman spectrometer (Horiba JOBIN YVON; HR 800).

4.3 Electrochemical measurements

The electrochemical tests were carried out using CR2025 coin-type cells, which were assembled in an argon-filled glovebox (Dellix, $[O_2]$ < 1 ppm, $[H_2O]$ < 1 ppm). The working electrodes were prepared by mixing the active material, carbon black (Super-P-Li) and binder (sodium carboxymethylcellulose, NaCMC) at a mass ratio of 7:2:1 using deionized water as solvent. After 24 h magnetic stirring at room temperature, the mixing slurry was pasted uniformly onto copper foil (D = 12.6 mm), then dried in a vacuum oven at 40 °C overnight. The mass loading of active materials in the anodes is about 1.5 mg/cm. Glass microfibers (Whatman), a circular Na tablets and 1 M $NaCF_3SO_3$ in DEGDME were employed as the separator, counter electrode and electrolyte, respectively. For comparison, the carbonate-based electrolytes including 1.0 M $NaClO_4$ in propylene carbonate (PC) with 5 wt.% fluoroethylene carbonate (FEC) and 1.0 M $NaPF_6$ in ethylene carbonate/ dimethyle carbonate (EC/DEC; v/v =1:1) were also used to investigate the cycle stability of as-prepared $NiSe_x$@C/CNTs-10h through assembling coin-type half-cells. CV and EIS were conducted on a CHI660D electrochemical workstation. Galvanostatic discharge/charge cycles were performed on a NEWARE battery tester within a voltage window of 0.5–2.9 V in a thermotank at 24 °C. The specific capacity was calculated based on the total weight of as-prepared composites in the electrode. To further estimate the electrochemical performance of as-prepared $NiSe_x$@C/CNTs-10h, flower-like NVP was used as cathodic materials to assemble NVP//$NiSe_x$@C/CNTs-10h full cells. Before the preparation of full cells, $NiSe_x$@C/CNTs-10h anodes were electrochemically activated for three cycles. Then NVP cathodes and activated $NiSe_x$@C/CNTs-10h anodes were paired in a weight ratio of 8:1 with 1.0 M $NaCF_3SO_3$ in DEGDME as electrolyte.

4.3 Calculation method

The first-principle calculation has been done with CASTEP planewave pseuopotential package [54]. An ultrasoft pseu-dopotential has been used with a cut-off energy of 450 eV. The supercell used are large than 15 Ang so only Gamma point was used for reciprocal space integration. Hubbard U term has been added on Ni with a U value of 4.5 eV to describe the localized semi-core d states [55]. The BFGS algorithm has been used to relax the structure with a residual force of less than 0.02 eV/Å [56].

Electronic Supplementary Material: Supplementary material (additional FESEM, TEM images, EDX, XRD patterns, crystal structures, XPS spectra, BET, EIS analysis, electrochemical characterizations and comparison tables) is available in the online version of this article at https://doi.org/10.1007/s12274-020-2848-z.

References

[1]   Hwang, J. Y.; Myung, S. T.; Sun, Y. K. Sodium-ion batteries: Present and future. *Chem. Soc. Rev.* **2017**, *46*, 3529–3614.

[2]   Kim, H.; Kim, H.; Ding, Z.; Lee, M. H.; Lim, K.; Yoon, G.; Kang, K. Recent progress in electrode materials for sodium-ion batteries. *Adv. Energy Mater.* **2016**, *6*, 1600943.

[3]   Xie, F. X.; Zhang, L.; Ye, C.; Jaroniec, M.; Qiao, S. Z. The application of hollow structured anodes for sodium-ion batteries: From simple to complex systems. *Adv. Mater.* **2019**, *31*, 1800492.

[4]   Liu, Y. Y.; Zhou, G. M.; Liu, K.; Cui, Y. Design of complex nano-materials for energy storage: Past success and future opportunity. *Acc. Chem. Res.* **2017**, *50*, 2895–2905.

[5]   Deng, J. Q.; Luo, W. B.; Chou, S. L.; Liu, H. K.; Dou, S. X. Sodium-ion batteries: From academic research to practical commercialization. *Adv. Energy Mater.* **2018**, *8*, 1701428.

[6]   Chen, S. Q.; Wu, C.; Shen, L. F.; Zhu, C. B.; Huang, Y. Y.; Xi, K.; Maier, J.; Yu, Y. Challenges and perspectives for NASICON-type electrode materials for advanced sodium-ion batteries. *Adv. Mater.* **2017**, *29*, 1700431.

[7]   Deng, J.; Gong, Q. F.; Ye, H. L.; Feng, K.; Zhou, J. H.; Zha, C. Y.; Wu, J. H.; Chen, J. M.; Zhong, J.; Li, Y. G. Rational synthesis and assembly of Ni_3S_4 nanorods for enhanced electrochemical sodium-ion

storage. *ACS Nano* **2018**, *12*, 1829–1836.

[8] Zhou, L. M.; Zhang, K.; Sheng, J. Z.; An, Q. Y.; Tao, Z. L.; Kang, Y. M.; Chen, J.; Mai, L. Q. Structural and chemical synergistic effect of CoS nanoparticles and porous carbon nanorods for high-performance sodium storage. *Nano Energy* **2017**, *35*, 281–289.

[9] Liu, D. H.; Li, W. H.; Zheng, Y. P.; Cui, Z.; Yan, X.; Liu, D. S.; Wang, J. W.; Zhang, Y.; Lü, H. Y.; Bai, F. Y. et al. *In situ* encapsulating α-MnS into N,S-codoped nanotube-like carbon as advanced anode material: α→β phase transition promoted cycling stability and superior Li/Na-storage performance in half/full cells. *Adv. Mater.* **2018**, *30*, 1706317.

[10] Chao, D. L.; Ouyang, B.; Liang, P.; Huong, T. T. T.; Jia, G. C.; Huang, H.; Xia, X. H.; Rawat, R. S.; Fan, H. J. C-plasma of hierarchical graphene survives SnS bundles for ultrastable and high volumetric Na-Ion storage. *Adv. Mater.* **2018**, *30*, 1804833.

[11] Wang, Q. H.; Zhang, W. C.; Guo, C.; Liu, Y. J.; Wang, C.; Guo, Z. P. *In Situ* construction of 3D interconnected FeS@Fe₃C@Graphitic carbon networks for high-performance sodium-ion batteries. *Adv. Funct. Mater.* **2017**, *27*, 1703390.

[12] Su, D. W.; Kretschmer, K.; Wang, G. X. Improved electrochemical performance of Na-Ion batteries in ether-based electrolytes: A case study of ZnS nanospheres. *Adv. Energy Mater.* **2016**, *6*, 1501785.

[13] Dong, S. H.; Li, C. X.; Ge, X. L.; Li, Z. Q.; Miao, X. G.; Yin, L. W. ZnS-Sb₂S₃@C core-double shell polyhedron structure derived from metal-organic framework as anodes for high performance sodium ion batteries. *ACS Nano* **2017**, *11*, 6474–6482.

[14] Hou, H. S.; Banks, C. E.; Jing, M. J.; Zhang, Y.; Ji, X. B. Carbon quantum dots and their derivative 3D porous carbon frameworks for sodium-ion batteries with ultralong cycle life. *Adv. Mater.* **2015**, *27*, 7861–7866.

[15] Hu, Z.; Liu, Q. N.; Chou, S. L.; Dou, S. X. Advances and challenges in metal sulfides/selenides for next-generation rechargeable sodium-ion batteries. *Adv. Mater.* **2017**, *29*, 1700606.

[16] Xi, K.; He, D. Q.; Harris, C.; Wang, Y. K.; Lai, C.; Li, H. L.; Coxon, P. R.; Ding, S. J.; Wang, C.; Kumar, R. V. Enhanced sulfur transformation by multifunctional FeS₂/FeS/S composites for high-volumetric capacity cathodes in lithium-sulfur batteries. *Adv. Sci.* **2019**, *6*, 1800815.

[17] Xi, K.; Chen, B. A.; Li, H. L.; Xie, R. S.; Gao, C. L.; Zhang, C.; Kumar, R. V.; Robertson, J. Soluble polysulphide sorption using carbon nanotube forest for enhancing cycle performance in a lithium–sulphur battery. *Nano Energy* **2015**, *12*, 538–546.

[18] Hu, X.; Jia, J. C.; Wang, G. X.; Chen, J. X.; Zhan, H. B.; Wen, Z. H. Reliable and general route to inverse opal structured nanohybrids of carbon-confined transition metal sulfides quantum dots for high-performance sodium storage. *Adv. Energy Mater.* **2018**, *8*, 1801452.

[19] Ge, P.; Hou, H. S.; Li, S. J.; Yang, L.; Ji, X. B. Tailoring rod-like FeSe₂ coated with nitrogen-doped carbon for high-performance sodium storage. *Adv. Funct. Mater.* **2018**, *28*, 1801765.

[20] Lu, S. Y.; Zhu, T. X.; Wu, H.; Wang, Y. K.; Li, J.; Abdelkader, A.; Xi, K.; Wang, W.; Li, Y. G.; Ding, S. J. et al. Construction of ultrafine ZnSe nanoparticles on/in amorphous carbon hollow nanospheres with high-power-density sodium storage. *Nano Energy* **2019**, *59*, 762–772.

[21] Wei, X. J.; Tang, C. J.; An, Q. Y.; Yan, M. Y.; Wang, X. P.; Hu, P.; Cai, X. Y.; Mai, L. Q. FeSe₂ clusters with excellent cyclability and rate capability for sodium-ion batteries. *Nano Res.* **2017**, *10*, 3202–3211.

[22] Liu, H.; Guo, H.; Liu, B. H.; Liang, M. F.; Lv, Z. L.; Adair, K. R.; Sun, X. L. Few-layer MoSe₂ nanosheets with expanded (002) planes confined in hollow carbon nanospheres for ultrahigh-performance Na-Ion batteries. *Adv. Funct. Mater.* **2018**, *28*, 1707480.

[23] Niu, F. E.; Yang, J.; Wang, N. N.; Zhang, D. P.; Fan, W. L.; Yang, J.; Qian, Y. T. MoSe₂-covered N,P-doped carbon nanosheets as a long-life and high-rate anode material for sodium-ion batteries. *Adv. Funct. Mater.* **2017**, *27*, 1700522.

[24] Tang, C. J.; Wei, X. J.; Cai, X. Y.; An, Q. Y.; Hu, P.; Sheng, J. Z.; Zhu, J. X.; Chou, S. L.; Wu, L. M.; Mai, L. Q. ZnSe microsphere/multiwalled carbon nanotube composites as high-rate and long-life anodes for sodium-ion batteries. *ACS Appl. Mater. Interfaces* **2018**, *10*, 19626–19632.

[25] Yi, Y. Y.; Sun, Z. T.; Li, C.; Tian, Z. N.; Lu, C.; Shao, Y. L.; Li, J.; Sun, J. Y.; Liu, Z. F. Designing 3D biomorphic nitrogen-doped MoSe₂/graphene composites toward high-performance potassium-ion capacitors. *Adv. Funct. Mater.* **2020**, *30*, 1903878.

[26] Xia, Z.; Sun, H.; He, X.; Sun, Z. T.; Lu, C.; Li, J.; Peng, Y.; Dou, S. X.; Sun, J. Y.; Liu, Z. F. *In situ* construction of CoSe₂@vertical-oriented graphene arrays as self-supporting electrodes for sodium-ion capacitors and electrocatalytic oxygen evolution. *Nano Energy* **2019**, *60*, 385–393.

[27] Lu, C.; Li, Z. Z.; Xia, Z.; Ci, H. N.; Cai, J. S.; Song, Y. Z.; Yu, L. H.; Yin, W. J.; Dou, S. X.; Sun, J. Y. et al. Confining MOF-derived SnSe nanoplatelets in nitrogen-doped graphene cages via direct CVD for durable sodium ion storage. *Nano Res.* **2019**, *12*, 3051–3058.

[28] Li, Y.; Xu, Y. H.; Wang, Z. H.; Bai, Y.; Zhang, K.; Dong, R. Q.; Gao, Y. N.; Ni, Q.; Wu, F.; Liu, Y. J. et al. Stable carbon–selenium bonds for enhanced performance in *Tremella*-like 2D chalcogenide battery anode. *Adv. Energy Mater.* **2018**, *8*, 1800927.

[29] Zhang, Y. F.; Pan, A. Q.; Ding, L.; Zhou, Z. L.; Wang, Y. P.; Niu, S. Y.; Liang, S. Q.; Cao, G. Z. Nitrogen-doped yolk-shell-structured CoSe/C dodecahedra for high-performance sodium ion batteries. *ACS Appl. Mater. Interfaces* **2017**, *9*, 3624–3633.

[30] Wu, C.; Jiang, Y.; Kopold, P.; van Aken, P. A.; Maier, J.; Yu, Y. Peapod-like carbon-encapsulated cobalt chalcogenide nanowires as cycle-stable and high-rate materials for sodium-ion anodes. *Adv. Mater.* **2016**, *28*, 7276–7283.

[31] Chen, Y. Y.; Ji, S. F.; Zhao, S.; Chen, W. X.; Dong, J. C.; Cheong, W. C.; Shen, R. A.; Wen, X. D.; Zheng, L. R.; Rykov, A. I. et al. Enhanced oxygen reduction with single-atomic-site iron catalysts for a zinc-air battery and hydrogen-air fuel cell. *Nat. Commun.* **2018**, *9*, 5422.

[32] Jagadeesh, R. V.; Murugesan, K.; Alshammari, A. S.; Neumann, H.; Pohl, M. M.; Radnik, J.; Beller, M. MOF-derived cobalt nanoparticles catalyze a general synthesis of amines. *Science* **2017**, *358*, 326–332.

[33] Sun, L. M.; Li, R.; Zhan, W. W.; Yuan, Y. S.; Wang, X. J.; Han, X. G.; Zhao, Y. L. Double-shelled hollow rods assembled from nitrogen/sulfur-codoped carbon coated indium oxide nanoparticles as excellent photocatalysts. *Nat. Commun.* **2019**, *10*, 2270.

[34] Du, M.; Song, D.; Huang, A. M.; Chen, R. X.; Jin, D. Q.; Rui, K.; Zhang, C.; Zhu, J. X.; Huang, W. Stereoselectively assembled Metal-Organic Framework (MOF) host for catalytic synthesis of carbon hybrids for alkaline-metal-ion batteries. *Angew. Chem., Int. Ed.* **2019**, *58*, 5307–5311.

[35] Wang, S. Z.; McGuirk, C. M.; d'Aquino, A.; Mason, J. A.; Mirkin, C. A. Metal-organic framework nanoparticles. *Adv. Mater.* **2018**, *30*, 1800202.

[36] Guan, B. Y.; Yu, X. Y.; Wu, H. B.; Lou, X. W. Complex nanostructures from materials based on metal-organic frameworks for electro-chemical energy storage and conversion. *Adv. Mater.* **2017**, *29*, 1703614.

[37] Kaneti, Y. V.; Tang, J.; Salunkhe, R. R.; Jiang, X. C.; Yu, A. B.; Wu, K. C. W.; Yamauchi, Y. Nanoarchitectured design of porous materials and nanocomposites from metal-organic frameworks. *Adv. Mater.* **2017**, *29*, 1604898.

[38] Park, S. K.; Kim, J. K.; Chan Kang, Y. Metal–organic framework-derived CoSe₂/(NiCo)Se₂ box-in-box hollow nanocubes with enhanced electrochemical properties for sodium-ion storage and hydrogen evolution. *J. Mater. Chem. A* **2017**, *5*, 18823–18830.

[39] Xi, K.; Cao, S.; Peng, X. Y.; Ducati, C.; Kumar, R. V.; Cheetham, A. K. Carbon with hierarchical pores from carbonized metal-organic frameworks for lithium sulphur batteries. *Chem. Commun.* **2013**, *49*, 2192–2194.

[40] Chen, R. J.; Zhao, T.; Tian, T.; Cao, S.; Coxon, P. R.; Xi, K.; Fairen-Jimenez, D.; Kumar, R. V.; Cheetham, A. K. Graphene-wrapped sulfur/metal organic framework-derived microporous carbon composite for lithium sulfur batteries. *APL Mater.* **2014**, *2*, 124109.

[41] Tang, Y. C.; Zhao, Z. B.; Hao, X. J.; Wang, Y. W.; Liu, Y.; Hou, Y. N.; Yang, Q.; Wang, X. Z; Qiu, J. S. Engineering hollow polyhedrons structured from carbon-coated CoSe₂ nanospheres bridged by CNTs with boosted sodium storage performance. *J. Mater. Chem. A* **2017**, *5*, 13591–13600.

[42] Zhang, J.; Wan, J. W.; Wang, J. Y.; Ren, H.; Yu, R. B.; Gu, L.; Liu, Y. L.; Feng, S. H.; Wang, D. Hollow multi-shelled structure with metal-organic-framework-derived coatings for enhanced lithium

storage. *Angew. Chem., Int. Ed.* **2019**, *58*, 5266–5271.

[43] Xu, X. J.; Liu, J.; Liu, J. W.; Ouyang, L. Z.; Hu, R. Z.; Wang, H.; Yang, L. C.; Zhu, M. A general Metal-Organic Framework (MOF)-derived selenidation strategy for *in situ* carbon-encapsulated metal selenides as high-rate anodes for Na-Ion batteries. *Adv. Funct. Mater.* **2018**, *28*, 1707573.

[44] Zou, F.; Chen, Y. M.; Liu, K. W.; Yu, Z. T.; Liang, W. F.; Bhaway, S. M.; Gao, M.; Zhu, Y. Metal organic frameworks derived hierarchical hollow NiO/Ni/Graphene composites for lithium and sodium storage. *ACS Nano* **2016**, *10*, 377–386.

[45] Guan, B. Y.; Yu, L.; Lou, X. W. A dual-metal–organic-framework derived electrocatalyst for oxygen reduction. *Energy Environ. Sci.* **2016**, *9*, 3092–3096.

[46] Meng, J. S.; Niu, C. J.; Xu, L. H.; Li, J. T.; Liu, X.; Wang, X. P.; Wu, Y. Z.; Xu, X. M.; Chen, W. Y.; Li, Q. et al. General oriented formation of carbon nanotubes from metal-organic frameworks. *J. Am. Chem. Soc.* **2017**, *139*, 8212–8221.

[47] Park, S. K.; Kim, J. K.; Kang, Y. C. Excellent sodium-ion storage performances of CoSe$_2$ nanoparticles embedded within N-doped porous graphitic carbon nanocube/carbon nanotube composite. *Chem. Eng. J.* **2017**, *328*, 546–555.

[48] Kong, S. F.; Dai, R. L.; Li, H.; Sun, W. W.; Wang, Y. Microwave hydrothermal synthesis of Ni-based metal–organic frameworks and their derived yolk–shell NiO for Li-Ion storage and supported ammonia borane for hydrogen desorption. *ACS Sustainable Chem. Eng.* **2015**, *3*, 1830–1838.

[49] Ou, X.; Li, J.; Zheng, F. H.; Wu, P.; Pan, Q. C.; Xiong, X. H.; Yang, C. H.; Liu, M. L. *In situ* X-ray diffraction characterization of NiSe$_2$ as a promising anode material for sodium ion batteries. *J. Power Sources* **2017**, *343*, 483–491.

[50] Zhu, S. H.; Li, Q. D.; Wei, Q. L.; Sun, R. M.; Liu, X. Q.; An, Q. Y.; Mai, L. Q. NiSe$_2$ nanooctahedra as an anode material for high-rate and long-life sodium-ion battery. *ACS Appl. Mater. Interfaces* **2017**, *9*, 311–316.

[51] Lu, S. Y; Zhu, T. X.; Li, Z. Y.; Pang, Y. C.; Shi, L.; Ding, S. J.; Gao, G. X. Ordered mesoporous carbon supported Ni$_3$V$_2$O$_8$ composites for lithium-ion batteries with long-term and high-rate performance. *J. Mater. Chem. A* **2018**, *6*, 7005–7013.

[52] Zhu, G. Y.; Chen, T.; Wang, L.; Ma, L. B.; Hu, Y.; Chen, R. P.; Wang, Y. R.; Wang, C. X.; Yan, W.; Tie, Z. X. et al. High energy density hybrid lithium-ion capacitor enabled by Co$_3$ZnC@N-doped carbon nanopolyhedra anode and microporous carbon cathode. *Energy Storage Mater.* **2018**, *14*, 246–252.

[53] Zhao, W. X.; Guo, C. X.; Li, C. M. Lychee-like FeS$_2$@FeSe$_2$ core–shell microspheres anode in sodium ion batteries for large capacity and ultralong cycle life. *J. Mater. Chem. A* **2017**, *5*, 19195–19202.

[54] Fang, G. Z.; Wu, Z. X.; Zhou, J.; Zhu, C. Y.; Cao, X. X.; Lin, T. Q.; Chen, Y. M.; Wang, C.; Pan, A. Q.; Liang, S. Q. Observation of pseudocapacitive effect and fast ion diffusion in bimetallic sulfides as an advanced sodium-ion battery Anode. *Adv. Energy Mater.* **2018**, *8*, 1703155.

[55] Fang, Y. J.; Yu, X. Y.; Lou, X. W. Formation of hierarchical Cu-doped CoSe$_2$ microboxes via sequential ion exchange for high-performance sodium-ion batteries. *Adv. Mater.* **2018**, *30*, 1706668.

[56] Liu, S. T.; Li, D.; Zhang, G. J.; Sun, D. D.; Zhou, J. S.; Song, H. H. Two-dimensional NiSe$_2$/N-Rich carbon nanocomposites derived from Ni-hexamine frameworks for superb Na-Ion storage. *ACS Appl. Mater. Interfaces* **2018**, *10*, 34193–34201.